



Article

Amorphous Carbon and Cyano-Group Self-Modified P-Doped g-C₃N₄ for Boosting Photocatalytic H₂ Evolution

Hang Gao ¹, Minghao Zhang ¹, Huixin Li ¹, Yiran Zhang ¹, Caixia Song ^{1,2,*}  and Debao Wang ^{1,*} 

¹ College of Chemistry and Molecular Engineering, Qingdao University of Science and Technology, Qingdao 266042, China

² College of Materials Science and Engineering, Qingdao University of Science and Technology, Qingdao 266042, China

* Correspondence: songcaixia@qust.edu.cn (C.S.); dbwang@qust.edu.cn (D.W.)

Abstract: Designing g-C₃N₄-based nanostructured photocatalysts is crucial to boosting their application in advancing clean energy and sustainable environmental solutions. In this study, cyano groups and amorphous carbon self-modified P-doped g-C₃N₄ (PCNx) photocatalysts were designed and prepared by one-pot calcination. Melamine phosphate was employed as a multifunctional precursor to simultaneously achieve P-doping and amorphous carbon/cyano group self-modification in the g-C₃N₄ photocatalyst. The molar ratio of urea to melamine phosphate regulates the content of amorphous carbon and cyano groups, which further enhances the conductivity of g-C₃N₄. Due to the high conductivity of amorphous carbon and cyano groups, the charge transfer process was further accelerated. As a result, the optimized P-doping and amorphous carbon/cyano-group in PCN2 photocatalyst led to an excellent H₂ production rate of 157.86 μmol·g^{−1}·h^{−1} under visible light, which is approximately 2.4 times and 3 times higher than those of CN and PCN. The work developed an alternative strategy for the construction of highly efficient g-C₃N₄-based photocatalysts.

Keywords: g-C₃N₄; cyano groups; amorphous carbon; self-modification; photocatalyst; hydrogen production



Citation: Gao, H.; Zhang, M.; Li, H.; Zhang, Y.; Song, C.; Wang, D.

Amorphous Carbon and Cyano-Group Self-Modified P-Doped g-C₃N₄ for Boosting Photocatalytic H₂ Evolution. *Catalysts* **2024**, *14*, 523. <https://doi.org/10.3390/catal14080523>

Academic Editors: Lei Ma, Piotr Kuśtrowski, Mohd Rafatullah, Stanisław Waclawek and Jean-François Lamonier

Received: 27 June 2024

Revised: 5 August 2024

Accepted: 10 August 2024

Published: 13 August 2024



Copyright: © 2024 by the authors. Licensee MDPI, Basel, Switzerland. This article is an open access article distributed under the terms and conditions of the Creative Commons Attribution (CC BY) license (<https://creativecommons.org/licenses/by/4.0/>).

1. Introduction

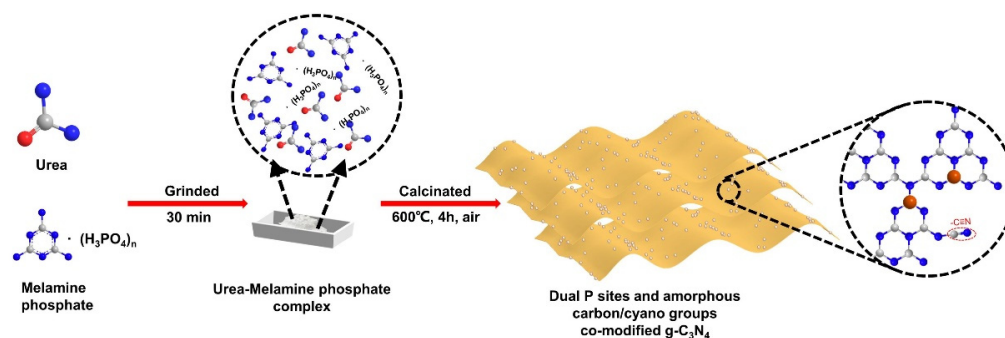
Hydrogen (H₂) has been widely accepted to be an environmentally friendly and renewable energy source because merely water and energy are the oxidation products of H₂, which makes it a promising, clean, and efficient fuel option to reduce environmental issues and fulfill the global energy demand [1]. Of the various options available, H₂ energy sources can be generated from water and sunlight, which offers one of the most promising pathways to achieve carbon neutrality by consuming two of the most abundant natural resources on earth [2]. Photocatalytic hydrogen evolution uses free solar energy to excite a semiconductor, generating photogenerated charges and catalyzing the H⁺ reduction. The key factor is to design a photocatalyst with excellent visible light response, cost-effective, and stable in practical application. Various semiconductor materials have been extensively researched to develop stable and high-performing photocatalysts for the production of hydrogen energy, including metal oxides, sulfides, and their composites, as well as non-metal compounds [3–8]. Among them, graphitic carbon nitride (g-C₃N₄)-based photocatalysts have gained intensive investigation due to their low cost, high stability, non-metallic properties, and suitable band gap (~2.7 eV) [9–11]. Unfortunately, single-component g-C₃N₄ shows lower photocatalytic H₂ production efficiency due to the rapid photocarrier recombination associated with its symmetry structure, which leads to the overlap of photogenerated electrons and holes [12]. Therefore, the preparation of g-C₃N₄-based photocatalysts with high photocatalytic hydrogen production performance still faces a tremendous challenge.

Until now, numerous approaches have been employed to overcome the intrinsic drawbacks, such as element doping and carbon material modification [13–16]. Element

doping, especially P element doping, can change the electrical structure of g-C₃N₄ due to unique electronegativity and valence electron structure, which improves photocatalytic performance. For example, Hammoud et al. prepared the P-doped g-C₃N₄ photocatalyst using NaH₂PO₄ dopant precursor, which exhibited increased visible light absorption and promoted charge-carrier separation [17]. Yu et al. prepared the P-doped photocatalyst by pre-hydrothermal and calcination processes. The introduction of P element effectively adjusted the band gap and accelerated the charge transfer separation. Furthermore, the surface defects were formed because of the P element doping, which provided more active sites for the photocatalytic hydrogen production reaction [18]. Sun et al. revealed that tuning the content of P element doping could modulate the electronic donor concentration, which regulated the Fermi level from below to above the doping level. Therefore, the photocarrier lifetime was prolonged when the doping state neared the Fermi level [19]. P element is preferred to replace a single C element to form a P-N bond. The formed P-N bond can act as a charge transfer bridge, which results in enhanced visible light absorption, more active sites, and efficient separation of photocarriers [20]. Recently, some research revealed that the photocatalytic performance is significantly influenced by the positions of P-element doped in the g-C₃N₄ network. For example, Yu et al. prepared dual P-doped site modified g-C₃N₄ for H₂O₂ production using two phosphorus dopants. The results indicated that dual P-site doping g-C₃N₄ exhibited higher photocatalytic performance than its single P-site counterpart because of its large surface area and more carrier transport channels [21].

Carbon materials with excellent conductivity have generally been used to strengthen the photocatalytic activity of the photocatalysts. For instance, Tian et al. found that amorphous carbon (a-C)-decorated g-C₃N₄ exhibited promoted performance for photocatalytic H₂ production, which was caused by the facilitated charge transfer efficiency due to the excellent conductivity of a-C [22]. Li et al. synthesized a carbon particle-decorated photocatalyst, which significantly accelerated the storage and transfer of electrons. The photocatalytic hydrogen production performance of the modified photocatalyst was remarkably enhanced [23]. Cyano groups can trap photogenerated electrons, which suppress charge recombination. For instance, Chang et al. reported that cyano groups, as stronger electron-withdrawing groups, could prevent the recombination of photocatalytic carriers, enhance the electron excitation from $n \rightarrow \pi^*$, and accelerate the H⁺ adsorption, which caused improved photocatalytic hydrogen production activity [24]. Other researchers successfully introduced the cyano groups on the backbone edge of g-C₃N₄. The cyano groups played important roles in the photocatalytic hydrogen reaction, which worked as electron capture centers to alter the band gap of g-C₃N₄, reducing the recombination rate of electron-hole pairs and accelerating the charge separation. Compared with single component g-C₃N₄, the photocatalytic hydrogen production activity was enhanced 13.5 times [25]. The modification of amorphous carbon and cyano groups generally requires supernumerary precursors. For instance, Xu et al. synthesized amorphous carbon-decorated g-C₃N₄ by calcining urea with glucose. The amorphous carbon in the interlayer was grown in situ, which contributed to more efficient charge transfer [26]. Huang et al. prepared cyano group-modified g-C₃N₄ using trithiocyanuric acid and melamine by calcination. Cyano groups enhanced the formation of medium basic sites and assisted the H₂ activation of Ru co-catalyst, leading to higher photocatalytic performance [27]. It is expected that the regulation of amorphous carbon and cyano groups could further enhance the photocatalytic activity of g-C₃N₄, and a detailed investigation is urgent.

In this study, urea and melamine phosphate were used as precursors to synthesize a self-modified g-C₃N₄ photocatalyst, which is schematically illustrated in Scheme 1. Melamine phosphate achieves P-site doping and self-modification of amorphous carbon/cyano groups. The in situ synthesized amorphous carbon and cyano groups promote the bulk-to-surface charge transfer. The molar ratio of urea modulates the concentration of amorphous carbon and cyano groups, which further promotes the conductivity of g-C₃N₄. Therefore, the g-C₃N₄ prepared from the dual precursors shows excellent photocatalytic hydrogen production activity.



Scheme 1. Schematic illustration for the preparation of PCNx photocatalysts.

2. Results and Discussions

2.1. Photocatalyst Characterization

To investigate the crystal structures of photocatalysts, the prepared samples were subjected to powder X-ray diffraction (XRD). As presented in Figure 1A, the distinct peak at around 27.9° observed in the CN, PCN, and PCN2 samples corresponded to the typical (002) crystal plane of $g\text{-C}_3\text{N}_4$ [28]. In addition to the (002) diffraction of $g\text{-C}_3\text{N}_4$, a broad and weak peak around 22.5° in the PCN and PCN2 samples was observed more clearly than in the CN sample, which may be caused by the P element doping and the formation of amorphous structure carbon [23,26]. CN exhibited a stronger (002) peak intensity, which represents the interfacial stacking reflection of the conjugated aromatic structure. For PCN and PCN2, the (002) peak remained the dominant diffraction, indicating the phase structure remained. However, the (002) peak intensity became weaker, which corresponded to the broken interlayer arrangement in the photocatalysts. At the same time, the peak intensity of amorphous carbon of PCN2 was slightly weaker than that of PCN, suggesting that the concentration of amorphous carbon decreased. Meanwhile, the characteristic peak of amorphous carbon in PCN2 was much broader than in PCN, which assigned a smaller particle size. The results indicate that the molar ratio of urea to melamine phosphate regulates the content of amorphous structures in the samples, which benefits photocatalytic performance.

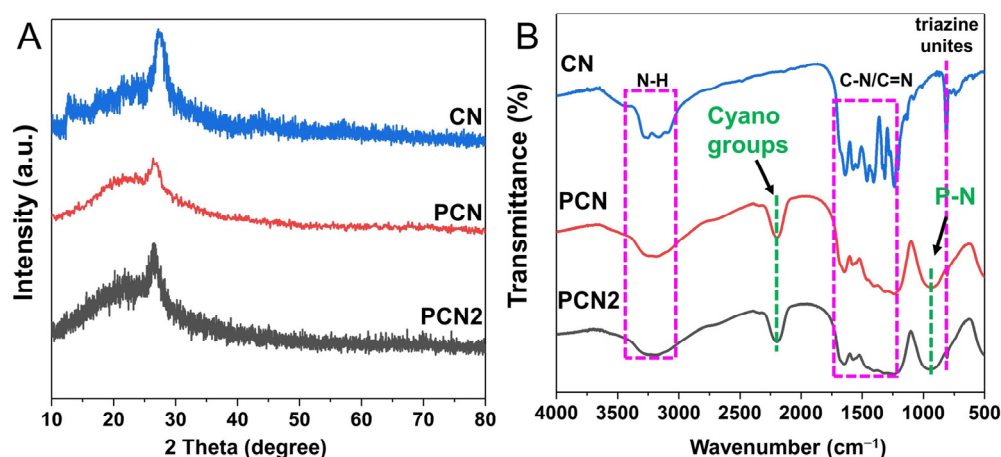


Figure 1. (A) XRD pattern and (B) FT-IR spectra of CN, PCN, and PCN2.

Fourier transform infrared (FT-IR) spectra were applied to estimate the molecular structures of CN, PCN, and PCN2. As reported in Figure 1B, a sharp peak in 802 cm^{-1} originated from the typical vibration of triazine units of $g\text{-C}_3\text{N}_4$ [29]. The absorption at $3400\text{--}3000\text{ cm}^{-1}$ was assigned to the stretching vibration of N-H. Additionally, the peak at about $1700\text{--}1200\text{ cm}^{-1}$ was ascribed to the typical C-N and C=N heterocycles characteristic stretching vibration pattern [30,31]. These characteristic peaks illustrated the formation of a typical $g\text{-C}_3\text{N}_4$ structure [32]. Impressively, a new peak at 2200 cm^{-1} was discovered

in PCN and PCN2, which corresponded to the cyano groups [33]. The peak intensities of cyano groups were reduced in PCN2, assessing that the tunable concentration could be achieved by adding urea. Furthermore, the vibration mode at 950 cm^{-1} discovered in PCN and PCN2 corresponded to the P-N bond, which proved that P replaced C atoms in the structure [34].

The morphology and nanostructure of PCN2 were determined by SEM, TEM, and HRTEM images. As shown in Figure 2A, PCN2 showed a typical nano-sheet stacking morphology. For the morphology comparison with PCN2, SEM images of both CN and PCN have been provided in Figure S1. Figure S1a shows the sheet-like structure of bulk $g\text{-C}_3\text{N}_4$, while PCN in Figure S1b possesses ultra-thin sheet structures as that of PCN2. TEM and HRTEM images further revealed the layered structure of PCN2, as shown in Figure 2B,C, which was consistent with the SEM spectrum. The inset of Figure 2C clearly presents the lattice fringe of $g\text{-C}_3\text{N}_4$ with a spacing of 0.33 nm [22,35]. The AFD image and element mappings in Figure 2D indicate the uniform distribution of C, N, and P elements in the PCN2 sample.

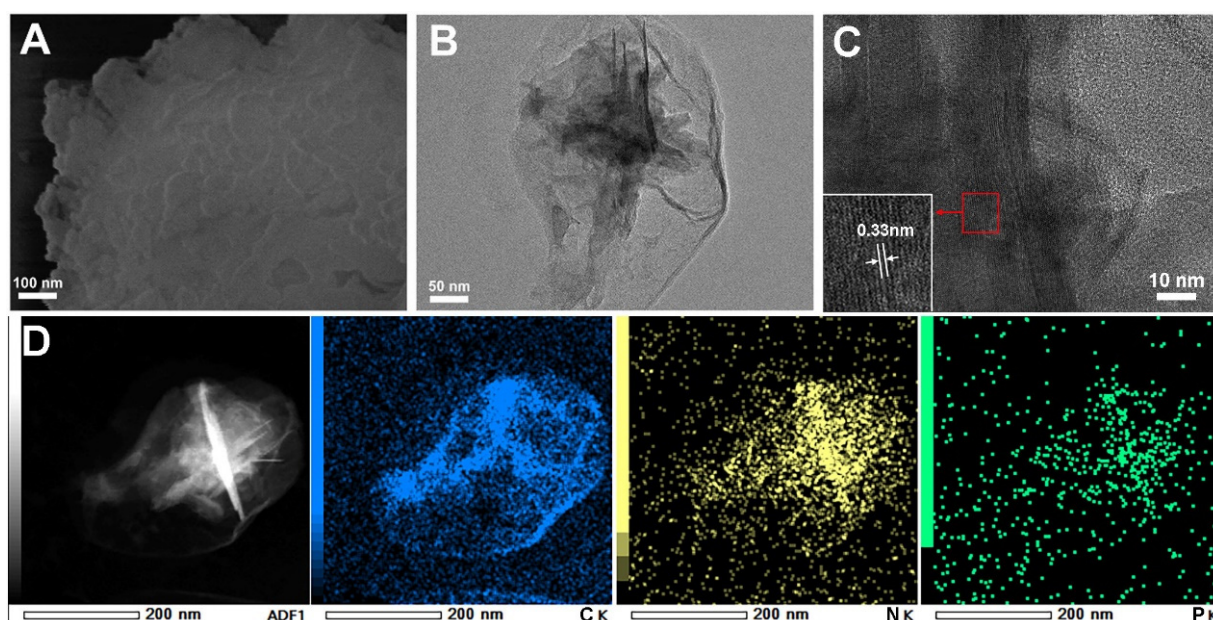


Figure 2. (A) SEM, (B) TEM, and (C) HRTEM images of PCN2; (D) AFD image and element mappings of PCN2.

In many instances, the catalytic activity of a photocatalyst is related to its specific surface area and pore structure. Therefore, the N_2 adsorption/desorption isotherms of PCN and PCN2 photocatalysts have been recorded. The specific surface areas were determined using the BET (Brunauer–Emmet–Teller) method and the pore diameters were analyzed through BJH (Barrett–Joyner–Halenda) method. As displayed in Figure S2, both photocatalysts present type-IV isotherms with a hysteresis loop, which implies the existence of mesopores in PCN and PCN2 [24]. The insets of Figure S2 confirm that both of them have a pore size distribution ranging from 2 nm to 10 nm . Calculated from N_2 adsorption/desorption isotherms, PCN possesses a surface area of $29.6\text{ m}^2\text{ g}^{-1}$ and pore diameters centered at 3.8 nm , while PCN2 has a surface area of $52.4\text{ m}^2\text{ g}^{-1}$ and pore diameters centered at 6.8 nm . It is evident that PCN possesses a higher BET surface area and a larger dominant pore diameter. This type of mesoporous structure allows for more effective penetration and absorption of light and offers more active sites for enhanced photocatalytic H_2 evolution activity of photocatalysts.

XPS measurements were applied to quantify the surface chemical composition of photocatalysts. Adventitious carbon (284.8 eV) was conducted to calibrate the binding energy scale. As shown in Figure 3A, the elements P, C, N, and O were detected in PCN

and PCN2. The surface element contents of PCN and PCN2 photocatalysts are listed in Table S1, further confirming the addition of urea could regulate the content of carbon and P-doping in the samples. Three peaks at 284.8 eV, 286.3 eV, and 288.5 eV were observed in C 1s spectra of PCN2 from Figure 3B, which could be assigned to amorphous carbon (C-C groups) and $\text{-C}\equiv\text{N}$ and N-C=N bonds [36–39], indicating the formation of cyano groups. The N 1s spectra could be deconvoluted into two diffraction peaks at 397.8 eV and 399.4 eV, as reported in Figure 3C, which belong to the C=N-C bond and $\text{sp}^2\text{ N}$ in N-(C)_3 bond [40,41]. The distinct characteristic peaks at around 133 eV and 134 eV in Figure 3D were attributed to the P-N and P=N coordination in the PCN and PCN2 samples, indicating that the P atoms have dual doping sites in aromatic rings [42,43]. The O1s spectra in Figure S3 have been fitted into two components at around 533.8 and 532.0 eV, which could be assigned to surface adsorbed oxygen species (such as water and oxygen) because the relative intensity of these peaks is constant [44]. All the results confirm that cyano-group self-modified P-doped $\text{g-C}_3\text{N}_4$ has been successfully prepared by employing urea and melamine phosphate as multifunctional precursors. The XPS data are in agreement with the above-discussed FT-IR results.

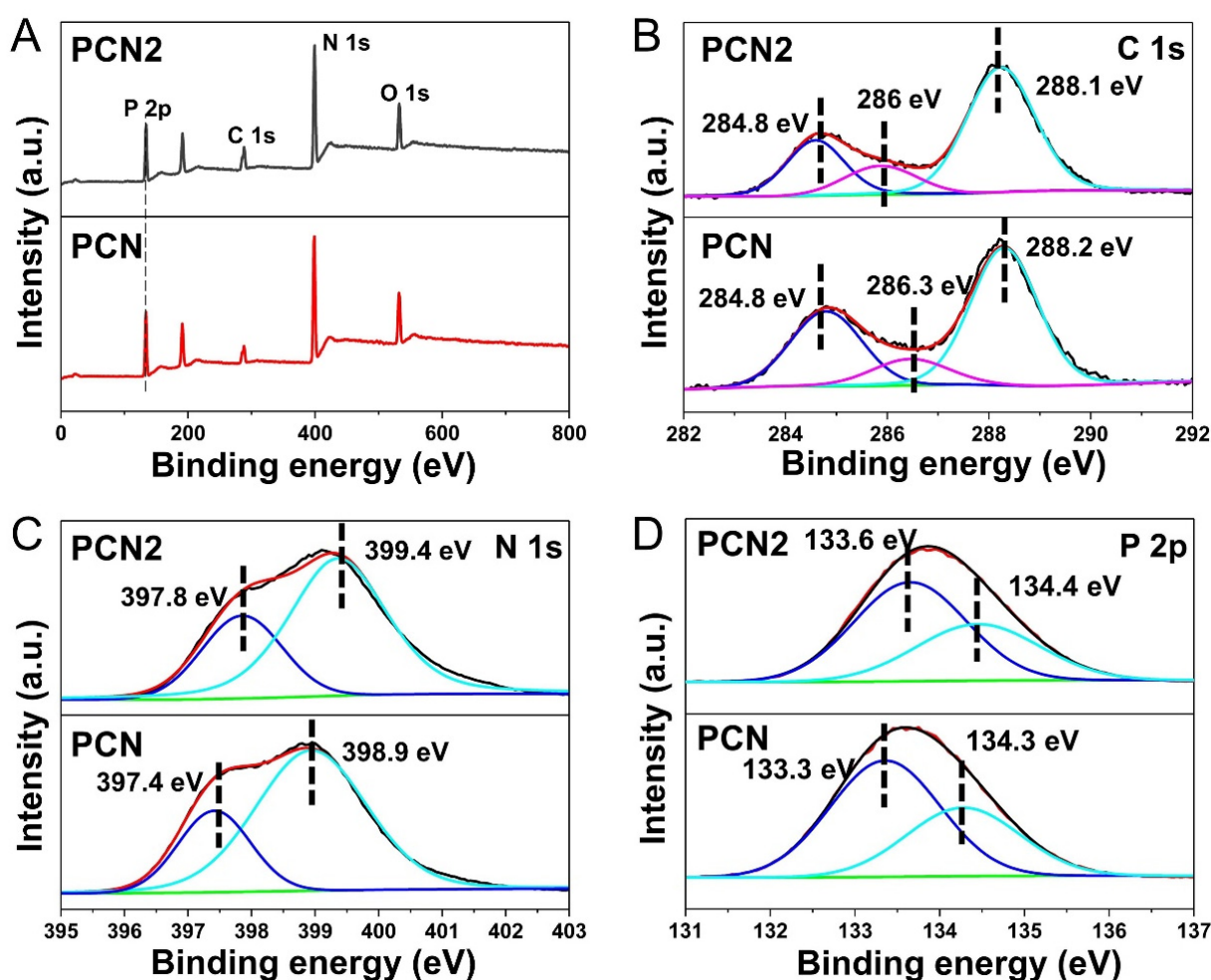


Figure 3. (A) XPS survey spectra, (B) C 1s, (C) N 1s, and (D) P 2p spectra of PCN and PCN2.

2.2. Photocatalytic Performance of Catalysts

The photocatalytic hydrogen activities of PCN, CN, and PCN_x were carried out with 10% TEOA as the sacrificial agent. 2 wt% Pt, as co-catalyst, was loaded onto the surface of the photocatalysts using a photo deposition method before the reaction. As shown in Figure 4A, the hydrogen production rate of PCN was 313.3 $\mu\text{mol g}^{-1}$, while that of CN was 395.1 $\mu\text{mol g}^{-1}$. The optimized PCN_x exhibited the highest photocat-

alytic hydrogen production rate compared to both CN and PCN after urea regulation, which were $755.04 \mu\text{mol g}^{-1}$ for PCN1, $947.16 \mu\text{mol g}^{-1}$ for PCN2, and $874.74 \mu\text{mol g}^{-1}$ for PCN3. PCN2 demonstrated the best photocatalytic hydrogen production rate of $157.86 \mu\text{mol g}^{-1} \text{ h}^{-1}$, as shown in Figure 4B, which was about 2.4 times and 3 times higher than those of CN and PCN, respectively. For comparison, the PCN2 without Pt co-catalyst can achieve a photocatalytic hydrogen production of $616.8 \mu\text{mol g}^{-1}$ and a hydrogen production rate of $102.8 \mu\text{mol g}^{-1} \text{ h}^{-1}$, which are even much higher than those of the PCN and CN with Pt co-catalyst.

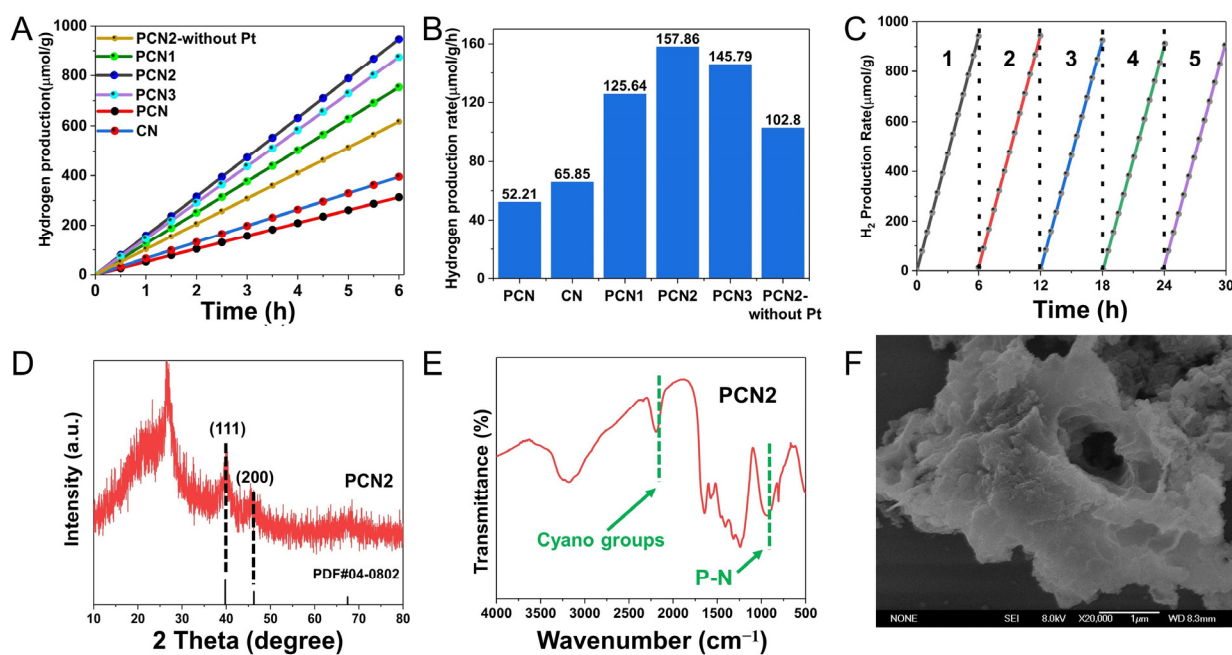


Figure 4. (A,B) Photocatalytic hydrogen production performances of PCN, CN, and PCNx; (C) recycling hydrogen evolution of PCN2; (D) XRD spectra, (E) FTIR, and (F) SEM of PCN2 after the reaction.

The stability of the photocatalyst was an important factor for industrial production and application. PCN2 was used as the photocatalyst to conduct the five cyclic experiments. As shown in Figure 4C, the photocatalytic hydrogen production just shows a slight drop and remains more than 95% after five-cycle experiments, indicating the good stability and reusability of the PCN2 photocatalyst. The stability of PCN2 was further identified using XRD, FTIR, and SEM. The characteristic peaks of $g\text{-C}_3\text{N}_4$ and amorphous carbon were still clearly detected in the XRD spectra of PCN2 after the reaction (Figure 4D). The peaks at 39.7° and 46.2° corresponded to the (111) and (200) crystal faces of the Pt co-catalyst, indicating the successful deposition of the Pt co-catalyst. Cyano groups and characteristic P-N bonds were also detected in the FTIR spectra, as shown in Figure 4E. PCN2 still retained the nanosheet morphology after the reaction, as shown in Figure 4F, demonstrating the high stability of the prepared photocatalyst. In order to further reveal the excellent performance of the prepared PCN2 photocatalyst, a comparison with previous results was outlined in Table 1. Obviously, the photocatalytic hydrogen production activity of PCN2 was superior to that of most CN-based photocatalysts, indicating the outstanding performance of PCN2.

Table 1. A comparison of the photocatalytic hydrogen production activity of PCN2 with that of other reported photocatalysts.

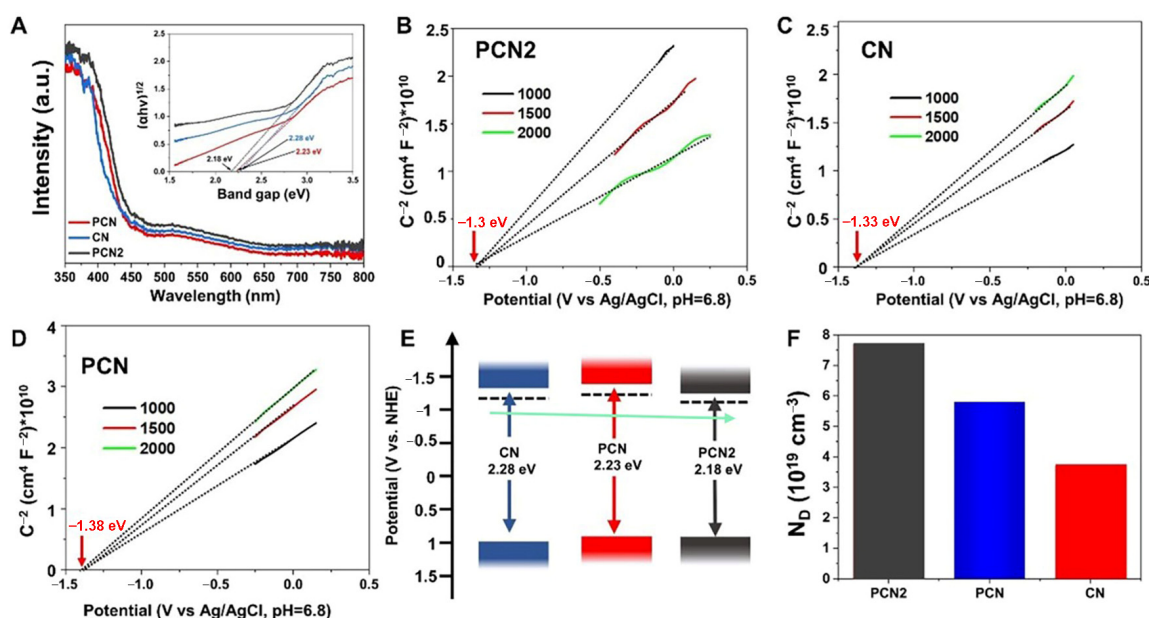
Catalysts	Light Source	Scavengers	Dosage of Photocatalyst	H ₂ Evolution Rate (μmol g ^{−1} h ^{−1})	Ref.
PCN2	300 W Xe lamp	TEOA	100 mg	157.86	This work
g-C ₃ N ₄ -Zn-1@Pt	250 W Xe lamp	TEOA	75 mg	78.7	[45]
g-C ₃ N ₄ /Ni ₂ P	300 W Xe lamp	TEOA	20 mg	82.5	[46]
LaFeO ₃ /g-C ₃ N ₄ /NiS	300 W Xe lamp	TEOA	100 mg	121	[47]
Eu/CN	300 W Xe lamp	TEOA	50 mg	128.8	[48]
CuO/CN	300 W LED lamp	TEOA	50 mg	130.1	[49]
WC/g-C ₃ N ₄	300 W Xe lamp	TEOA	50 mg	146.1	[50]
g-C ₃ N ₄ /MeTMC-COP	300 W Xe lamp	TEOA	10 mg	11.8	[51]
CuO/pCN	400 W Xe lamp	TEOA	50 mg	30	[52]
p-CNGT	300 W Xe lamp	TEOA	30 mg	33.1	[53]
Co ₃ O ₄ @g-C ₃ N ₄ /CNFs	300 W Xe lamp	TEOA	5 mg	67.17	[54]

2.3. Mechanism of Photocatalytic H₂ Production

UV-vis diffuse reflectance spectra (UV-vis DRS) were recorded to evaluate the light absorption properties of the photocatalysts. According to Figure 5A, CN, PCN, and PCN2 had intrinsic absorption edges around 450 nm. PCN2 showed more progressive visible light absorption ability than CN and PCN, indicating more effective use of solar energy. The band gap energies (E_g) of PCN, CN, and PCN2 were calculated by the following formula [55]:

$$(\alpha h\nu)^n = A(h\nu - E_g)$$

where α denotes the absorption coefficient, and h and ν represent Planck's constant and incident light frequency, respectively. A is the proportionality constant, and E_g represents band gap energy. n takes the value of 1/2 for indirect band gap semiconductor. Then, the band gaps of CN, PCN, and PCN2 were estimated to be 2.28 eV, 2.23 eV, and 2.18 eV, respectively, as shown in the inset of Figure 5A.

**Figure 5.** (A) UV-vis DRS spectra and band gap (inset) of PCN, CN, and PCN2; (B) Mott-Schottky spectra of PCN2; (C) Mott-Schottky spectra of CN; (D) Mott-Schottky spectra of PCN; (E) energy band alignments of PCN, CN, and PCN2; (F) N_D of PCN, CN, and PCN2.

Mott–Schottky spectra were conducted to determine the semiconductor type and flat band potentials of the photocatalysts. As depicted in Figure 5B–D, CN, PCN, and PCN2 all showed an n-type slope, and the flat band potentials were estimated to be -1.33 eV, -1.38 eV, and -1.3 eV (V vs. Ag/AgCl, pH = 6.8), respectively. According to the equation [56]

$$E_{(\text{vs. NHE, pH}=0)} = E_{(\text{vs. Ag/AgCl})} + 0.059 \times \text{pH} + E_{(\text{Ag/AgCl})}$$

The flat band potentials of CN, PCN, and PCN2 were converted to normal hydrogen electrodes (vs. NHE) for -1.13 eV, -1.18 eV, and -1.1 eV, respectively. The lower flat band potential also represents the better electrical conductivity of PCN2 [57]. The CB potentials were generally more negative than the flat band by about -0.2 eV [58]. Therefore, the CB potentials of CN, PCN, and PCN2 were determined to be -1.33 eV, -1.38 eV, and -1.3 eV (vs. NHE), respectively. The bandgap alignments of the photocatalysts are illustrated in Figure 5E, which provided evidence for charge transfer. The charge carrier density (N_D) reflects the electron density of the photocatalysts, and a higher N_D value indicates a greater electron density in the photocatalyst. N_D could be calculated by applying the following equation [59]:

$$N_D = \left(\frac{2}{\epsilon \epsilon_0 e_0} \right) \left[\frac{d(1/C^2)}{dV} \right]^{-1}$$

which ϵ represents the dielectric constant ($\epsilon_{\text{g-C}_3\text{N}_4} = 2$) [60], ϵ_0 corresponds to the vacuum permittivity ($8.86 \times 10^{-12} \text{ F m}^{-1}$), e_0 is the electronic charge unit ($1.6 \times 10^{-19} \text{ C}$), and V is the potential. As shown in Figure 5F, the values of N_D were calculated to be $7.7 \times 10^{19} \text{ cm}^{-3}$ for PCN2, $5.8 \times 10^{19} \text{ cm}^{-3}$ for PCN, and $3.7 \times 10^{19} \text{ cm}^{-3}$ for CN, indicating the highest electron density of PCN2. According to the above analysis, the photocatalyst prepared from the dual precursors exhibited a narrower band gap and a higher electron density.

The photocarrier separation performances of the fabricated photocatalysts were investigated by transient photocurrent response measurement (I-t) and electrochemical impedance spectra (EIS) tests. Higher photocurrent density of photocatalysts indicated faster charge transfer capability. As shown in Figure 6A, PCN2 showed higher photocurrent intensity than CN and PCN, demonstrating an improved photocarrier separation efficiency. A smaller arc radius in EIS spectra usually suggests a lower electron transfer resistance. As shown in Figure 6B, the resistivity of PCN2 was $1.7 \times 10^5 \Omega$, which was much smaller than those of PCN ($12 \times 10^5 \Omega$) and CN ($75 \times 10^5 \Omega$). The resistivities of the prepared samples decreased in the order PCN2 < CN < PCN, demonstrating the reduced charge transfer resistance of PCN2. Photoluminescence (PL) was analyzed to determine the recombination rate of photocarriers. Lower fluorescence intensity indicated an enhanced separation rate of the photocarriers. Obviously, PCN2 showed the lowest emission intensity, as shown in Figure 6C, proving the inhibited photocarrier recombination ability. Time-resolved photoluminescence (TRPL) was implemented to investigate the photocarrier separation process and the lifetime of the photocatalysts. It was determined from Figure 6D that PCN2 exhibited the longest lifetime compared to PCN and CN, which demonstrated the promoted photocarrier separation rate [61].

According to the above discussion, a possible mechanism of the enhanced photocatalytic hydrogen production mechanism is proposed, as shown in Figure 7. Photoelectrons are promoted from the valence band of PCN to the conduction band under visible light. Then the photoelectrons are quickly transferred from the bulk to the surface because of the high conductivity of amorphous carbon and cyano groups. The molar ratio of urea to melamine phosphate regulates the content of amorphous carbon and cyano groups for the optimum property. The photoelectrons at the surface are then captured by Pt for photocatalytic hydrogen production. The synergetic effect of the ultra-thin structure and P-doping could supply a large quantity of active sites for photocatalytic hydrogen production [62]. As a result, PCN2 shows enhanced photocatalytic hydrogen production activity.

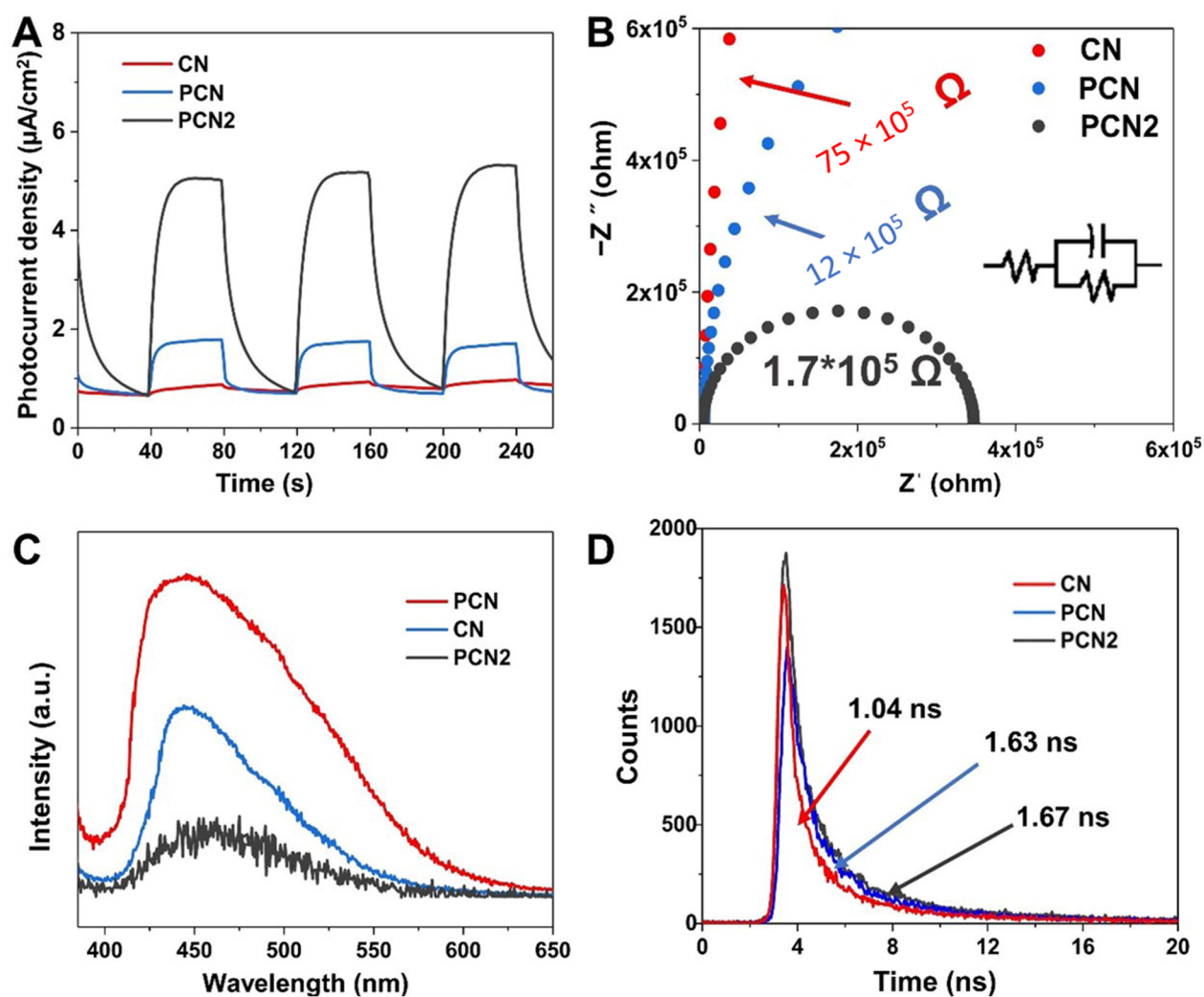


Figure 6. (A) I-t curves, (B) EIS spectra, (C) PL, and (D) TRPL of PCN, CN, and PCN2.

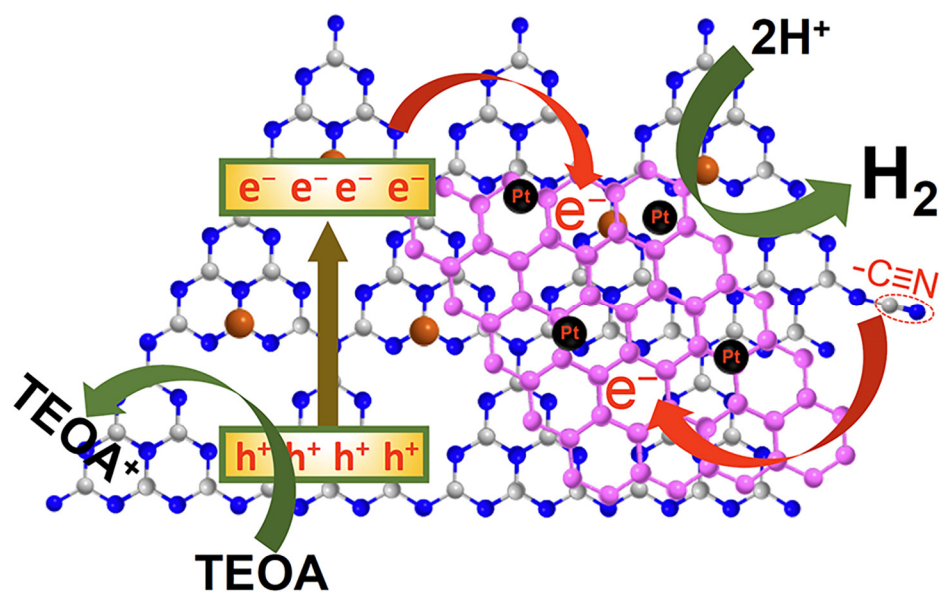


Figure 7. Possible mechanism for the photocatalytic hydrogen production performance of PCN2.

3. Materials and Methods

3.1. Materials

Melamine phosphate ($\text{C}_3\text{H}_6\text{N}_6(\text{H}_3\text{PO}_4)_n$, 99%) was purchased from Shanghai Macklin Biochemical Co., Ltd. (Shanghai, China); Urea ($\text{CH}_4\text{N}_2\text{O}$, 99%), ethanol ($\text{CH}_3\text{CH}_2\text{OH}$, 99%), triethanolamine (TEOA, 99%), and H_2PtCl_6 (99%) were purchased from Sinopharm Chemical Reagent Co., Ltd. (Shanghai, China). All chemical reagents in this report were of analytical grade and employed without further treatment.

3.2. Fabrication of Photocatalysts

Preparation of PCNx: Amorphous carbon and cyano-group self-modified g- C_3N_4 photocatalysts were prepared using the one-pot thermal polymerization method, which was schematically illustrated in Scheme 1. Typically, 5 mmol melamine phosphate and different amounts of urea were adequately ground in a mortar for 30 min. The resultant powders were transferred to a porcelain boat covered with aluminum foil and heated at 600 °C for 4 h with a heating rate of 10 °C/min under air. The obtained yellow products were washed with deionized water and ethanol and then dried at 60 °C. The final photocatalysts obtained with different amounts of urea (6.6 mmol, 10.8 mmol, and 15 mmol) were labeled as PCN1, PCN2, and PCN3.

For comparison, 5 mmol melamine phosphate or 83.3 mmol urea was subjected to fabricate photocatalysts from a single precursor with the same procedure. The obtained samples were expressed as PCN and CN, respectively. The yield of prepared samples was outlined in Table S2 (supporting information). All the samples have a yield higher than 74%.

3.3. Characterizations of Photocatalysts

A D-MAX 2500/PC powder X-ray diffraction diffractometer (XRD) (Rigaku Corporation, Tokyo, Japan) was used to identify the crystal structures of synthesized carbon nitride composite photocatalysts with Cu K α radiation at 40 kV and 150 mA. A Nicolet IS50 (ThermoFisher Scientific, Waltham, MA, USA) spectrometer was used to record Fourier-transform infrared (FTIR) spectra in the form of KBr pellets. Scanning electron microscopy (SEM, JSM-6700F microscope, JEOL Ltd., Tokyo, Japan) was carried out to determine the morphologies of photocatalysts. A JEM-F200 transmission electron microscope (TEM) (JEOL Ltd., Tokyo, Japan) was used to obtain TEM and high-resolution TEM (HRTEM) images and element mappings. An ESCALAB 250XI X-ray photoelectron spectrometer (XPS) (Thermo Fisher Scientific Inc., Waltham, MA, USA) was applied to analyze the surface chemical states of the photocatalysts using Al-K α radiation. Photoluminescence (PL) measurements were conducted on an LS-55 fluorescence spectrophotometer (Perkin Elmer, Waltham, MA, USA) under the excitation wavelength of 375 nm. A Perkin-Elmer Lambda 750 spectrophotometer (Perkin Elmer, Waltham, MA, USA) was employed to collect the UV-Vis Diffuse reflectance spectra (DRS) of the prepared composites. Time-resolved photoluminescence (TRPL) was measured by a fluorescence lifetime spectrophotometer (Edinburgh Instruments FS5, Edinburgh Instruments Ltd., Livingston, UK) with an excitation wavelength of 375 nm. N_2 desorption adsorption isotherms were recorded on a N_2 adsorption analyzer (Micromeritics ASAP 2460 Version 3.01).

Detailed photoelectrochemical measurements were supplied as the electronic supporting information.

3.4. Photocatalytic Hydrogen Production Measurement

The photocatalytic hydrogen production experiments were performed in a sealable quartz vessel with the irradiation of a CEL-HXF 300 Xe lamp (CEAULIGHT, Beijing, China, $\lambda > 420$ nm). Typically, 100 mg photocatalysts were dispersed in 100 mL aqueous solution, which contained 10% vol (10 mL) TEOA as the sacrificial agent. 2 wt% Pt was photo-deposition on the photocatalyst. 0.266 mL H_2PtCl_6 (1 g/50 mL) was added to the system and irradiated for 1 h before the reaction. The reaction temperature was maintained at

7 °C through cyclical cooling water. The quartz vessel was vacuumed thoroughly. The H₂ content was determined using an online gas chromatograph (Agilent 7890A, Hong Kong, China) equipped with a thermal conductivity detector and a 4 m 5 Å molecular sieve column. High-purity N₂ was used as the carrier gas. The produced H₂ was analyzed at an interval of every 30 min.

The photocatalytic cyclic stability measurement was performed by batch experiments. After each reaction, the photocatalyst was centrifuged and dried at 60 °C and then reused in 100 mL fresh aqueous solution containing 10% TEOA (10 mL) for the next 6 h reaction.

4. Conclusions

In summary, P-doped g-C₃N₄ with self-modified amorphous carbon and cyano groups was prepared using a one-pot method. Melamine phosphate was used as an important precursor to prepare P-doped g-C₃N₄, which simultaneously caused the self-modification of amorphous carbon and cyano groups. Both amorphous carbon and cyano groups could enhance the photocarrier transfer from the bulk to the surface because of their high conductivity. Urea regulated the concentration and structural properties of amorphous carbon and cyano groups, which further enhanced the conductivity and visible light absorption of the photocatalyst. Therefore, PCN2 exhibited excellent photocatalytic hydrogen production activity compared to PCN and CN, which was about 157.86 μmol·g^{−1}·h^{−1}. The work developed an alternative strategy for the construction of high-performance g-C₃N₄ photocatalysts.

Supplementary Materials: The following supporting information can be downloaded at <https://www.mdpi.com/article/10.3390/catal14080523/s1>: photoelectrochemical measurements of the catalysts and some experimental results (Figures S1–S3, Tables S1 and S2).

Author Contributions: Conceptualization, H.G. and C.S.; methodology, H.G.; validation, M.Z., H.L. and Y.Z.; investigation, H.G. and M.Z.; writing—original draft preparation, H.G.; writing—review and editing, C.S. and D.W.; supervision, C.S. and D.W. All authors have read and agreed to the published version of the manuscript.

Funding: This research was funded by the National Natural Science Foundation of China (grant number 52072194).

Data Availability Statement: The data presented in this study are available upon request from the authors.

Conflicts of Interest: The authors declare no conflicts of interest.

References

1. Zhou, P.; Navid, I.A.; Ma, Y.; Xiao, Y.; Wang, P.; Ye, Z.; Zhou, B.; Sun, K.; Mi, Z. Solar-to-hydrogen efficiency of more than 9% in photocatalytic water splitting. *Nature* **2023**, *613*, 66–70. [CrossRef]
2. Hisatomi, T.; Domen, K. Reaction systems for solar hydrogen production via water splitting with particulate semiconductor photocatalysts. *Nat. Catal.* **2019**, *2*, 387–399. [CrossRef]
3. Raza, A.; Zhang, Y.; Cassinese, A.; Li, G. Engineered 2D Metal Oxides for Photocatalysis as Environmental Remediation: A Theoretical Perspective. *Catalysts* **2022**, *12*, 1613. [CrossRef]
4. Mamiyev, Z.; Balayeva, N.O. Metal Sulfide Photocatalysts for Hydrogen Generation: A Review of Recent Advances. *Catalysts* **2022**, *12*, 1316. [CrossRef]
5. Mohamed, R.M.; Shawky, A. Promoted visible-light-driven H₂ production over hydrothermally synthesized YVO₄ nanorods coupled with Pt/AgInS₂ nanospheres. *Ceram. Int.* **2023**, *49*, 15015–15023. [CrossRef]
6. Benlembarek, M.; Salhi, N.; Benrabaa, R.; Djaballah, A.M.; Boulahouache, A.; Trari, M. Synthesis, physical and electrochemical properties of the spinel CoFe₂O₄: Application to the photocatalytic hydrogen production. *Int. J. Hydrogen Energy* **2022**, *47*, 9239–9247. [CrossRef]
7. Alhaddad, M.; El-Hout, S.I. Hydrothermal fabrication of visible-light photoactive Ag₂O/BaSnO₃ nanocomposite and its application in hydrogen production. *Opt. Mater.* **2023**, *146*, 114517. [CrossRef]
8. Starukh, H.; Praus, P. Doping of Graphitic Carbon Nitride with Non-Metal Elements and Its Applications in Photocatalysis. *Catalysts* **2020**, *10*, 1119. [CrossRef]
9. Liu, J.; Liu, Y.; Liu, N.; Han, Y.; Zhang, X.; Huang, H.; Lifshitz, Y.; Lee, S.; Zhong, J.; Kang, Z. Metal-free efficient photocatalyst for stable visible water splitting via a two-electron pathway. *Science* **2015**, *347*, 970–974. [CrossRef] [PubMed]

10. He, B.; Zhang, S.; Zhang, Y.; Li, G.; Zhang, B.; Ma, W.; Rao, B.; Song, R.; Zhang, L.; Zhang, Y.; et al. ortho-Terphenylene Viologens with Through-Space Conjugation for Enhanced Photocatalytic Oxidative Coupling and Hydrogen Evolution. *J. Am. Chem. Soc.* **2022**, *144*, 4422–4430. [[CrossRef](#)] [[PubMed](#)]
11. Xie, Z.-K.; Jia, Y.J.; Huang, Y.Y.; Xu, D.B.; Wu, X.J.; Chen, M.; Shi, W.D. Near-Infrared Light-Driven Photocatalytic Reforming Lignocellulose into H₂ and Chemicals over Heterogeneous Carbon Nitride. *ACS Catal.* **2023**, *13*, 13768–13776. [[CrossRef](#)]
12. Yang, Z.; Yuan, M.; Cheng, Z.; Liu, B.; Ma, Z.; Ma, J.; Zhang, J.; Ma, X.; Ma, P.; Lin, J. Defect-Repaired g-C₃N₄ Nanosheets: Elevating the Efficacy of Sonodynamic Cancer Therapy Through Enhanced Charge Carrier Migration. *Angew. Chem. Int. Ed.* **2024**, *63*, e202401758. [[CrossRef](#)] [[PubMed](#)]
13. Liu, Y.; Sun, Y.; Zhao, E.; Yang, W.; Lin, J.; Zhong, Q.; Qi, H.; Deng, A.; Yang, S.; Zhang, H.; et al. Atomically Dispersed Silver-Cobalt Dual-Metal Sites Synergistically Promoting Photocatalytic Hydrogen Evolution. *Adv. Funct. Mater.* **2023**, *33*, 2301840. [[CrossRef](#)]
14. Zhu, X.; Yang, F.; Liu, J.; Zhou, G.; Chen, D.; Liu, Z.; Fang, J. Design and Architecture of P-O Co-Doped Porous g-C₃N₄ by Supramolecular Self-Assembly for Enhanced Hydrogen Evolution. *Catalysts* **2022**, *12*, 1583. [[CrossRef](#)]
15. Santiago-Aliste, A.; Sánchez-Hernández, E.; Andrés-Juan, C.; Chamorro-Posada, P.; Antorrena, G.; Martín-Gil, J.; Martín-Ramos, P. F,O,S-Codoped Graphitic Carbon Nitride as an Efficient Photocatalyst for the Synthesis of Benzoxazoles and Benzimidazoles. *Catalysts* **2023**, *13*, 385. [[CrossRef](#)]
16. Tian, C.; Li, C.; Zhao, C.; Liu, D.; He, X. A Novel Synthetic 3D Interconnected Porous Carbon-Rich Graphitic Carbon Nitride for Boosting Visible Light Photocatalytic Hydrogen Production and Dye Contaminant Degradation. *Catalysts* **2023**, *13*, 1345. [[CrossRef](#)]
17. Hammoud, L.; Marchal, C.; Caps, V.; Toufaily, J.; Hamieh, T.; Keller, V. Influence of low level of non-metal doping on g-C₃N₄ performance for H₂ production from water under solar light irradiation. *Int. J. Hydrogen Energy* **2024**, *51*, 285–300. [[CrossRef](#)]
18. Yu, D.; Jia, T.; Deng, Z.; Wei, Q.; Wang, K.; Chen, L.; Wang, P.; Cui, J. One-Dimensional P-Doped Graphitic Carbon Nitride Tube: Facile Synthesis, Effect of Doping Concentration, and Enhanced Mechanism for Photocatalytic Hydrogen Evolution. *Nanomaterials* **2022**, *12*, 1759. [[CrossRef](#)]
19. Sun, S.C.; Peng, B.; Song, Y.; Liu, B.; Song, H.T.; Lin, W. Boosting photoelectron transfer by Fermi and doping levels regulation in carbon nitride towards efficient solar-driven hydrogen production. *Chem. Eng. J.* **2024**, *495*, 153547. [[CrossRef](#)]
20. Gao, F.; Xiao, H.; Yang, J.; Luan, X.; Fang, D.; Yang, L.; Zi, J.; Lian, Z. Modulation of electronic density in ultrathin g-C₃N₄ for enhanced photocatalytic hydrogen evolution through an efficient hydrogen spillover pathway. *Appl. Catal. B* **2024**, *341*, 123334. [[CrossRef](#)]
21. Yu, G.; Gong, K.; Xing, C.; Hu, L.; Huang, H.; Gao, L.; Wang, D.; Li, X. Dual P-doped-site modified porous g-C₃N₄ achieves high dissociation and mobility efficiency for photocatalytic H₂O₂ production. *Chem. Eng. J.* **2023**, *461*, 142140. [[CrossRef](#)]
22. Tian, X.; Xue, M.; Yang, X.; Jiang, D.; Yuan, Y. Up-cycling of waste paper for increased photo-catalytic hydrogen generation of graphitic carbon nitride under visible light exposure. *J. Taiwan Inst. Chem. Eng.* **2021**, *127*, 259–264. [[CrossRef](#)]
23. Li, H.; Wang, G.; Zhang, X.; Jin, Z. Based on amorphous carbon C@ZnxCd1-xS/Co₃O₄ composite for efficient photocatalytic hydrogen evolution. *Int. J. Hydrogen Energy* **2020**, *45*, 8405–8417. [[CrossRef](#)]
24. Chang, X.; Fan, H.; Zhu, S.; Lei, L.; Wu, X.; Feng, C.; Wang, W.; Ma, L. Engineering doping and defect in graphitic carbon nitride by one-pot method for enhanced photocatalytic hydrogen evolution. *Ceram. Int.* **2023**, *49*, 6729–6738. [[CrossRef](#)]
25. Li, K.Q.; Jiang, Y.Q.; Li, Y.D.; Wang, Z.; Liu, X.; Wang, P.; Xia, D.B.; Fan, R.Q.; Lin, K.F.; Yang, Y.L. In situ preparation of graphitic carbon nitride bonded with cyano groups for enhanced photocatalytic activity. *Int. J. Hydrogen Energy* **2020**, *45*, 9683–9694. [[CrossRef](#)]
26. Xu, Q.; Cheng, B.; Yu, J.; Liu, G. Making co-condensed amorphous carbon/g-C₃N₄ composites with improved visible-light photocatalytic H₂-production performance using Pt as cocatalyst. *Carbon* **2017**, *118*, 241–249. [[CrossRef](#)]
27. Huang, T.; Wang, R.; Zhang, J.; Wang, J.; Ge, H.; Ren, J.; Zheng, Z. Cyano group modified graphitic carbon nitride supported Ru nanoparticles for enhanced CO₂ methanation. *Chem. Eng. J.* **2023**, *467*, 143469. [[CrossRef](#)]
28. Gao, Y.; Wang, Y.; Sun, R.; Luo, Y.; Xin, L.; Wang, D. Interfacial hot electron injection in Cu₂O/MXene-g-C₃N₄ p-n heterojunction for efficient photocatalytic CO₂ reduction. *Colloids Surf. A Physicochem. Eng. Aspects* **2024**, *684*, 133236. [[CrossRef](#)]
29. Hoang, T.V.A.; Nguyen, P.A.; Shin, E.W. Effect of Morphological Modification over g-C₃N₄ on Photocatalytic Hydrogen Evolution Performance of g-C₃N₄-Pt Photocatalysts. *Catalysts* **2023**, *13*, 92. [[CrossRef](#)]
30. Saman, F.; Bahruji, H.; Mahadi, A.H.; Ling, C.H.S. Pd/g-C₃N₄ photocatalyst for hydrogen production: Role of experimental condition for Schottky barrier. *Fuel* **2023**, *349*, 128725. [[CrossRef](#)]
31. Chang, X.; Fan, H.; Lei, L.; Wu, X.; Wang, W.; Ma, L. Generation Mechanism of the Defects in g-C₃N₄ Synthesized in N₂ Atmosphere and the Method for Improving Photocatalysis Activity. *Catalysts* **2023**, *13*, 269. [[CrossRef](#)]
32. Liu, X.; Wang, S.; Yang, F.; Zhang, Y.; Yan, L.; Li, K.; Guo, H.; Yan, J.; Lin, J. Construction of Au/g-C₃N₄/ZnIn₂S₄ plasma photocatalyst heterojunction composite with 3D hierarchical microarchitecture for visible-light-driven hydrogen production. *Int. J. Hydrogen Energy* **2022**, *47*, 2900–2913. [[CrossRef](#)]
33. Yuan, J.; Tian, N.; Zhu, Z.; Yu, W.; Li, M.; Zhang, Y.; Huang, H. P, K doped crystalline g-C₃N₄ grafted with cyano groups for efficient visible-light-driven H₂O₂ evolution. *Chem. Eng. J.* **2023**, *467*, 143379. [[CrossRef](#)]
34. Yu, G.; Gong, K.; Hu, L.; Xing, C.; Hu, Y.; Wang, D.; Li, X. Controllably solar-driven C–C coupling organic synthesis integrated with H₂ production over P-doped g-C₃N₄ with NiS nanoparticles modification. *Appl. Mater. Today* **2023**, *32*, 101794. [[CrossRef](#)]

35. Sun, H.; Shi, Y.; Shi, W.; Guo, F. High-crystalline/amorphous g-C₃N₄ S-scheme homojunction for boosted photocatalytic H₂ production in water/simulated seawater: Interfacial charge transfer and mechanism insight. *Appl. Surf. Sci.* **2022**, *593*, 153281. [CrossRef]
36. Katsumata, H.; Islam Molla, M.A.; Islam, J.B.; Tateishi, I.; Furukawa, M.; Kaneco, S. Dual Z-scheme heterojunction g-C₃N₄/Ag₃PO₄/AgBr photocatalyst with enhanced visible-light photocatalytic activity. *Ceram. Int.* **2022**, *48*, 21898–21905. [CrossRef]
37. Mkhalid, I.A.; Mohamed, R.M.; Alhaddad, M.; Basaleh, A.; Al-Hajji, L.A.; Ismail, A.A. Green synthesis of porous Cu₂ZnSnS₄/g-C₃N₄ heterostructured for promoted photocatalytic degradation of trichloroethylene. *Ceram. Int.* **2022**, *48*, 11736–11746. [CrossRef]
38. Roškarič, M.; Zavašnik, J.; Zámbo, D.; Kotnik, T.; Kovačič, S.; Žerjav, G.; Pintar, A. Optimization Method Based on Simplex for Surface Area Improved Photocatalytic Performance of g-C₃N₄. *ACS Catal.* **2023**, *13*, 13282–13300. [CrossRef]
39. Nguyen, T.B.; Ho, P.N.T.; Huang, C.P.; Doong, R.-a.; Chen, L.; Chen, C.-W.; Dong, C.-D. Peroxymonosulfate-assisted visible light sensitive 0D/3D Z-scheme NiCo₂O₄@g-C₃N₄ photocatalyst for effective degradation of ibuprofen in water. *Chem. Eng. J.* **2023**, *478*, 147332. [CrossRef]
40. Kwon, N.H.; Park, J.; Jin, X.; Kim, S.-J.; Kim, H.; Hwang, S.-J. Defect-Regulated Two-Dimensional Superlattice of Holey g-C₃N₄-TiO₂ Nanohybrids: Contrasting Influence of Vacancy Content on Hybridization Impact and Photocatalyst Performance. *ACS Nano* **2023**, *17*, 23732–23745. [CrossRef] [PubMed]
41. Gao, H.; Zhang, M.; Liu, X.; Li, H.; Yu, G.; Wang, D. Ni₇S₆ decorated g-C₃N₄/graphene oxide composites for enhanced visible light photocatalytic hydrogen evolution. *Diamond Relat. Mater.* **2024**, *143*, 110869. [CrossRef]
42. Lv, S.; Ng, Y.H.; Zhu, R.; Li, S.; Wu, C.; Liu, Y.; Zhang, Y.; Jing, L.; Deng, J.; Dai, H. Phosphorus vapor assisted preparation of P-doped ultrathin hollow g-C₃N₄ sphere for efficient solar-to-hydrogen conversion. *Appl. Catal. B* **2021**, *297*, 120438. [CrossRef]
43. Raziq, F.; Hayat, A.; Humayun, M.; Baburao Mane, S.K.; Faheem, M.B.; Ali, A.; Zhao, Y.; Han, S.; Cai, C.; Li, W.; et al. Photocatalytic solar fuel production and environmental remediation through experimental and DFT based research on CdSe-QDs-coupled P-doped-g-C₃N₄ composites. *Appl. Catal. B* **2020**, *270*, 118867. [CrossRef]
44. Xu, C.; Wu, S.; Xiong, G.; Guo, X.; Yang, H.; Yan, J.; Cen, K.; Bo, Z.; Ostrikov, K. Nanoconfined fusion of g-C₃N₄ within edge-rich vertically oriented graphene hierarchical networks for high-performance photocatalytic hydrogen evolution utilizing superhydrophilic and superaerophobic responses in seawater. *Appl. Catal. B* **2021**, *280*, 119461. [CrossRef]
45. Fuentez-Torres, M.O.; Ortiz-Chi, F.; Espinosa-González, C.G.; Aleman, M.; Cervantes-Urbe, A.; Torres-Torres, J.G.; Kesarla, M.K.; Collins-Martínez, V.; Godavarthi, S.; Martínez-Gómez, L. Facile Synthesis of Zn Doped g-C₃N₄ for Enhanced Visible Light Driven Photocatalytic Hydrogen Production. *Top. Catal.* **2020**, *64*, 65–72. [CrossRef]
46. Ye, P.; Liu, X.; Iocozzia, J.; Yuan, Y.; Gu, L.; Xu, G.; Lin, Z. A highly stable non-noble metal Ni₂P co-catalyst for increased H₂ generation by g-C₃N₄ under visible light irradiation. *J. Mater. Chem. A* **2017**, *5*, 8493–8498. [CrossRef]
47. Xu, K.; Xu, H.; Feng, G.; Feng, J. Photocatalytic hydrogen evolution performance of NiS cocatalyst modified LaFeO₃/g-C₃N₄ heterojunctions. *New J. Chem.* **2017**, *41*, 14602–14609. [CrossRef]
48. Li, Y.; Lai, C.; Zhong, J.; Li, J. Largely elevated photocatalytic hydrogen generation over Eu doped g-C₃N₄ photocatalyst. *Int. J. Hydrogen Energy* **2023**, *48*, 24356–24368. [CrossRef]
49. Zhang, Q.; Li, Y.; Zhong, J.; Li, J. Facile construction of CuO/g-C₃N₄ heterojunctions with promoted photocatalytic hydrogen generation behaviors. *Fuel* **2023**, *353*, 129224. [CrossRef]
50. He, K.; Xie, J.; Yang, Z.; Shen, R.; Fang, Y.; Ma, S.; Chen, X.; Li, X. Earth-abundant WC nanoparticles as an active noble-metal-free co-catalyst for the highly boosted photocatalytic H₂ production over g-C₃N₄ nanosheets under visible light. *Catal. Sci. Technol.* **2017**, *7*, 1193–1202. [CrossRef]
51. Cao, L.; Qiao, S.; Li, X.; Li, Q. Synthesis and photocatalytic performance of g-C₃N₄/MeTMC-COP composite photocatalyst. *Front. Chem.* **2023**, *11*, 1138789. [CrossRef] [PubMed]
52. Raza, A.; Haidry, A.A.; Amin, T.; Hussain, A.A.; Shah, S.A.M.H.; Ahsan, M. Boosting the water splitting and hydrogen production of S-scheme fabricated porous g-C₃N₄ modified with CuO. *Diamond Relat. Mater.* **2024**, *141*, 110703. [CrossRef]
53. Li, W.; Ma, Q.; Wang, X.; Chu, X.-S.; Wang, F.; Wang, X.-C.; Wang, C.-Y. Enhanced photoresponse and fast charge transfer: Three-dimensional macroporous g-C₃N₄/GO-TiO₂ nanostructure for hydrogen evolution. *J. Mater. Chem. A* **2020**, *8*, 19533–19543. [CrossRef]
54. He, R.; Liang, H.; Li, C.; Bai, J. Enhanced photocatalytic hydrogen production over Co₃O₄@g-C₃N₄ p-n junction adhering on one-dimensional carbon fiber. *Colloids Surf. A* **2020**, *586*, 124200. [CrossRef]
55. Liu, T.; Hao, L.; Bai, L.; Liu, J.; Zhang, Y.; Tian, N.; Huang, H. Z-scheme junction Bi₂O₂(NO₃)(OH)/g-C₃N₄ for promoting CO₂ photoreduction. *Chem. Eng. J.* **2022**, *429*, 132268. [CrossRef]
56. Yang, Y.; Zeng, G.; Huang, D.; Zhang, C.; He, D.; Zhou, C.; Wang, W.; Xiong, W.; Li, X.; Li, B.; et al. Molecular engineering of polymeric carbon nitride for highly efficient photocatalytic oxytetracycline degradation and H₂O₂ production. *Appl. Catal. B* **2020**, *272*, 118970. [CrossRef]
57. Liang, Q.; Li, Z.; Huang, Z.H.; Kang, F.; Yang, Q.H. Holey Graphitic Carbon Nitride Nanosheets with Carbon Vacancies for Highly Improved Photocatalytic Hydrogen Production. *Adv. Funct. Mater.* **2015**, *25*, 6885–6892. [CrossRef]

58. Wang, Y.; Liu, X.; Liu, J.; Han, B.; Hu, X.; Yang, F.; Xu, Z.; Li, Y.; Jia, S.; Li, Z.; et al. Carbon Quantum Dot Implanted Graphite Carbon Nitride Nanotubes: Excellent Charge Separation and Enhanced Photocatalytic Hydrogen Evolution. *Angew. Chem. Int. Ed.* **2018**, *57*, 5765–5771. [[CrossRef](#)]
59. Liang, H.; Liu, B.J.; Tang, B.; Zhu, S.C.; Li, S.; Ge, X.Z.; Li, J.L.; Zhu, J.R.; Xiao, F.X. Atomically Precise Metal Nanocluster-Mediated Photocatalysis. *ACS Catal.* **2022**, *12*, 4216–4226. [[CrossRef](#)]
60. Liu, X.W.; Lin, J.H.; Jong, W.J.; Shih, H.C. The effect of pressure control on a thermally stable a-C:N thin film with low dielectric constant by electron cyclotron resonance-plasma. *Thin Solid Films* **2002**, *409*, 178–184. [[CrossRef](#)]
61. Chandra, M.; Guharoy, U.; Pradhan, D. Boosting the Photocatalytic H₂ Evolution and Benzylamine Oxidation using 2D/1D g-C₃N₄/TiO₂ Nanoheterojunction. *ACS Appl. Mater. Interfaces* **2022**, *14*, 22122–22137. [[CrossRef](#)]
62. Su, C.; Zhou, Y.; Zhang, L.; Yu, X.; Gao, S.; Sun, X.; Cheng, C.; Liu, Q.; Yang, J. Enhanced n→ π^* electron transition of porous P-doped g-C₃N₄ nanosheets for improved photocatalytic H₂ evolution performance. *Ceram. Int.* **2020**, *46*, 8444–8451. [[CrossRef](#)]

Disclaimer/Publisher’s Note: The statements, opinions and data contained in all publications are solely those of the individual author(s) and contributor(s) and not of MDPI and/or the editor(s). MDPI and/or the editor(s) disclaim responsibility for any injury to people or property resulting from any ideas, methods, instructions or products referred to in the content.